

Article

Study of the Effects of Er Doping on the Physical Properties of CdSe Thin Films

Yuliana de Jesús Acosta-Silva ^{1,*}, Luis A. Godínez ², Manuel Toledano-Ayala ¹, Rosendo Lozada-Morales ³, Orlando Zelaya-Angel ¹ and Arturo Méndez-López ^{1,*}

¹ División de Investigación y Posgrado, Facultad de Ingeniería, Universidad Autónoma de Querétaro, Centro Universitario, Querétaro 76010, Mexico

² Centro de Investigación en Química para la Economía Circular, CIQEC, Facultad de Química, Universidad Autónoma de Querétaro, Centro Universitario, Querétaro 76010, Mexico

³ Facultad de Ciencias Físico-Matemáticas, Benemérita Universidad Autónoma de Puebla, Puebla 72570, Mexico

* Correspondence: yuliana.dejesus.acosta@uaq.mx (Y.d.J.A.-S.); arturo.mendez@uaq.mx (A.M.-L.)

Abstract: Erbium-doped cadmium selenide thin films grown on 7059 Corning glass by means of a chemical bath at 80 °C were prepared. Doping was performed by adding an aqueous Er(NO₃)₃·H₂O dilution to the CdSe growth solution. The volume of Er doping solution was varied to obtain different Er concentration (*x* at%). Thus, in the Cd_{1-*x*}Er_{*x*}Se samples, the *x* values obtained were in the 0.0–7.8 at% interval. The set of the CdSe:Er thin films synthesized in the hexagonal wurtzite (WZ) crystalline phase are characterized by lattice parameters (*a* and *c*) that increase until *x* = 2.4% and that subsequently decrease as the concentration of *x* increases. Therefore, in the primitive unit cell volume (UC), the same effect was observed. Physical parameters such as nanocrystal size, direct band gap (*E_g*), and optical longitudinal vibrational phonon on the other hand, shift in an opposite way to that of UC as a function of *x*. All the samples exhibit photoluminescence (PL) emission which consists of a single broad band in the 1.3 ≤ *hν* ≤ 2.5 eV range (954 ≥ λ ≥ 496 nm), where the maximum of the PL-band shift depends on *x* in the same way as the former parameters. The PL band intensity shows a singular behavior since it increases as *x* augments but exhibits a strong decreasing trend in the intermediate region of the *x* range. Dark d.c. conductivity experiences a high increase with the lower *x* value, however, it gradually decreases as *x* increases, which suggests that the Er³⁺ ions are not only located in Cd²⁺ sites, but also in interstitial sites and at the surface. Different physical properties are correlated among them and discussed considering information from similar reports in the literature.

Keywords: CdSe nanocrystalline films; Er doping; CdSe:Er; CdSe photoluminescence; softening-hardening of phonons



Citation: Acosta-Silva, Y.d.J.; Godínez, L.A.; Toledano-Ayala, M.; Lozada-Morales, R.; Zelaya-Angel, O.; Méndez-López, A. Study of the Effects of Er Doping on the Physical Properties of CdSe Thin Films. *Magnetochemistry* **2023**, *9*, 107. <https://doi.org/10.3390/magnetochemistry9040107>

Academic Editors: Cătălin-Daniel Constantinescu and Lucian Petrescu

Received: 22 December 2022

Revised: 7 April 2023

Accepted: 11 April 2023

Published: 14 April 2023



Copyright: © 2023 by the authors. Licensee MDPI, Basel, Switzerland. This article is an open access article distributed under the terms and conditions of the Creative Commons Attribution (CC BY) license (<https://creativecommons.org/licenses/by/4.0/>).

1. Introduction

The wide implementation of thin films in various applications, prepared with compound semiconductors of the IIA-VIB group is due to their excellent characteristics; therefore, these compounds have attracted the attention of several research groups around the world [1,2]. Due to the compatibility in the synthesis of stoichiometric and non-stoichiometric compounds, the cadmoselite or cadmium selenide (CdSe) is a particularly attractive metal selenide from the II–VI group [3]. Its high absorption coefficient, appropriate band gap of 1.74 eV (which is close to the ideal band gap desired for an appropriate absorber layer), high electron affinity, elevated photosensitivity, and n-type conductivity, makes it one of the prominent competitors among Cd-based chalcogenides of the II–VI group [4–6]. Cadmium selenide is therefore an interesting semiconductor material that has been used as a model substrate to design, prepare and pursue novel applications such as semiconductor nanostructures [7], luminescent nanocrystals [8], phase transformations [9], vibrational modes [10] and colloidal luminescent monolayers [11], among others. In most

cases, CdSe exhibits n-type conductivity, which is dependent on its growing dynamics and on the development of vacancies. The n-type conductivity of CdSe films is caused by the Se vacancies, but the p-type conductivity may be caused by an Se surplus [6]. The CdSe material primarily exhibits cubic and hexagonal phases of crystallization and a combination of the cubic and hexagonal phases could arise during crystallization [6,12]. Several reports on the synthesis, properties and potential applications of CdSe have been published [13–15] and in the specific field of synthesis, new techniques to prepare chemically grown nanostructured CdSe films have been discovered. Among these, thermolysis of Cd and Se reagents [16], green methods [17], reverse micelle assisted hydrothermal [18] and rapid microwave synthesis [19], stand out as approaches to synthesize materials that can be used to prepare composite structures such as polymerized CdSe nanocrystals (NCs) [20], organic-inorganic hybrid CdSe NCs [21], CdSe-polymer fibers [22] and biocompatible CdSe-ZnS NCs [23]. These novel CdSe arrangements have been explored for applications in semiconductor nanostructure technology [24,25], food science [26] biologic images [27], agriculture [28] and DNA studies [29], among others.

The intrinsic CdSe nanobelts (NBs) exhibits an extremely high resistivity of $1 \times 10^{13} \Omega \text{ cm}$ and thus leads to its low conductivity [30]. In order to further expand its usage, it is necessary to adjust the carrier concentration and then mediate its bandgap. Several researchers intentionally introduced defects by doping and thus changed carrier concentrations to enhance its electro-optical properties [31–36]. Up to now, doping has resulted in optical, electronic and transport control as well as in spintronic properties of the semiconductor materials [37]. For example, Mg-doped CdSe can modulate its optical bandgap and makes possible light response in the whole visible range [38]. Sahu et al. doped CdSe nanocrystals with Ag impurities and investigated their optical and electrical properties. They observed that doping leads not only to dramatic changes but surprising complexity. The addition of just a few Ag atoms per nanocrystal causes a large enhancement in the fluorescence. While Ag was expected to be a substitutional acceptor, nonmonotonic trends in the fluorescence and Fermi level suggest that Ag changes from an interstitial (n-type) to a substitutional (p-type) impurity with increased doping [8].

In the case of rare earth (RE) element doping, interesting results have been obtained using CdSe as the semiconductor substrate. While CdSe:Y³⁺ for example, has been used for luminescence enhancement [39] and CdSe:Gd for potential optical and MR imaging [40], CdSe:Eu has been found to be an efficient photocatalytic material [41]. The morphological, structural, optical and other properties of a host lattice can be improved by gradual and systematic addition of various dopants [42,43]. On the other hand, erbium is another rare earth element used as impurity in optical amplifiers because of its high capacity to supply both high gain and high at-saturation output. The Er³⁺ ion is also an active lasing element. Therefore, Er³⁺ has become one of the most interesting topics of research due to $^4I_{9/2} \rightarrow ^4I_{15/2}$ and $^4I_{11/2} \rightarrow ^4I_{13/2}$ transitions [44], and these characteristic properties open up a new line of research for these materials due to the intra Er³⁺ 4f shell transition from its first excited state ($^4I_{3/2}$) to the ground state ($^4I_{5/2}$) [45]. In this context, the aim of the present work is to study some of the morphological, structural and optical properties of Er³⁺-doped CdSe thin films in order to obtain crystalline films. CdSe thin films were grown using the chemical bath (CB) method. In this way, Er³⁺ ions were efficiently incorporated into the semiconductor CdSe hexagonal wurtzite (WZ) crystalline phase with no important distortion of the lattice structure. Er³⁺ ions in the CdSe hexagonal wurtzite lattice are expected to occupy Cd²⁺ sites to produce an n-type CdSe doped substrate and in this work, the Er³⁺ doping values fall within the 0.0–7.8 at% interval. The WZ unit cell parameters, crystal size, vibrational modes, energy band gap, luminescence spectra and dark conductivity experience changes depending, as expected, on the Er concentration. The variation in these parameters and properties are discussed on the basis of the correlation of the experimental data obtained and of the information from similar works in the literature.

2. Experimental

Nanocrystalline CdSe:Er thin films were deposited on Corning 7059 glass substrates at 80 ± 1 °C. The glass substrates were cleaned by immersion in water for a couple of hours, and successive ultrasonic treatment using trichloroethylene, acetone, and deionized distilled water. Finally, the glass substrates were dried under a stream of pure N₂. The solutions employed in the growth of the CdSe:Er layers were: CdCl₂ 0.02 M, KOH 0.05 M, NH₄NO₃ 1.5 M, CSe(NH₂)₂ 0.02 M, and Er(NO₃)₃·3H₂O 0.5 M. The total volume of the growing solution, $V_T = 100$ mL, consists of the volume solution V_{CdSe} for CdSe plus the volume solution, V_{Er} , containing the doping Er chemical: $V_{\text{CdSe}} + V_{\text{Er}} = V_T = 100$ mL. $V_R = (V_{\text{Er}}/V_T)100\%$ on the other hand, corresponds to the relative volume, and different V_R values were chosen within the 1.0% to 25% interval in order to obtain eight different doping levels. The growing time was one hour for all the film depositions.

The average thickness (τ) of the films correspond to 200 ± 10 nm as measured with a KLA TENCO P-15 profilometer. Optical transmittance spectra were obtained using a UNICAM 8700 spectrophotometer. X-ray diffraction (XRD) patterns were measured using a Rigaku D/max-2100 diffractometer (CuK α radiation, $\lambda = 0.15406$ nm). High resolution (HR-TEM) images were registered in a Transmission Electron Microscope (TEM) Jeol 2010 working at 200 KeV, in which thin layers of the CdSe films were detached from the substrate and supported on TEM-grids. The selected area for electron diffraction (SAED) was performed at the camera length, $L_{\frac{1}{4}}=20$ cm. Measurements of the atomic concentration of elements were obtained by means of energy dispersion spectroscopy (EDS) utilizing a Voyager II X-ray quantitative microanalysis in an1100/1110 EDX system from Noran Instruments. Photoluminescence (PL) measurements were obtained using a 0.5 m Jovin-Ivon double spectrograph, employing as the excitation source the 441.6 nm (2.808 eV) line of an Omnicrome 2056 He-Cd laser with 35 mW of power. Raman spectra were obtained by means of a microRaman spectrometer (Jobin Yvon, model Labram) using the 632.8 nm laser line from a He-Ne laser. Finally, dark electrical conductivity measurements were obtained in vacuum using the two points method and sign of carriers (n) by thermoelectric power. The essential drawback of the usual two-point method arises from the approximation of the intrinsic drain voltage by the external applied drain bias. This means that high series resistances can induce significant errors in the lifetime evaluation [46]. All the characterization measurements were carried out at room temperature (RT).

3. Results and Discussion

The CdSe:Er thin films prepared as described in the experimental section, appear bright and smooth to the naked eye, as can be seen from inspection of insets (i) and (ii) of Figure 1, which correspond to a doped ($V_R = 15\%$) and undoped samples, respectively. Figure 1 also exhibits the Er concentration measured by means of EDS, where each data point is an average value of ten measurements. As it can be observed in Figure 1, the EDS data (in at%) vs. V_R plot, roughly follows a linear relationship. In the Cd_{1-x}Er_xSe doped samples, the Er concentration (x) varied within the $0 \leq x \leq 7.8$ at% range.

Nanocrystallites corresponding to the Cd_{1-x}Er_xSe WZ structure for $x = 4.6$ at% can be seen in the TEM image of Figure 1b. The crystalline [002] planes of the WZ phase can also be observed, and the (002) interplanar spacing (IS) was determined as 0.35 ± 0.01 nm, which can be associated to the standard IS value 0.3505 nm of the [002] planes in WZ-CdSe (JCPDS CAS No. 08-0459). The inset of Figure 1b exhibits the first diffraction rings of the WZ-CdSe structure as well as the SAED pattern of the sample where the nanocrystalline character of the film is confirmed.

The hexagonal wurtzite structure of the CdSe samples in the crystalline phase obtained from the diffractograms of Figure 2A can be seen for two representative samples prepared with different doping levels ($x = 5.5$ and 0.6 at%). The asterisks in the diffractograms mark where the XRD reflections of Er₂O₃ should be present [47,48]; however, most of the peaks showed low intensity. Er₂O₃ has been reported to appear as another phase when CdSe nanocrystals are obtained from molecular precursors [49] and when GaN:Er films are

prepared using MOCVD [50]. As it was observed for the CB method and in the preparation of Si by different methods [51], in these synthesis techniques, oxygen is captured by Er^{3+} ions and the resulting Er_2O_3 oxide has for instance, been observed in Er doped ZnO NCs prepared using the sol-gel method [48].

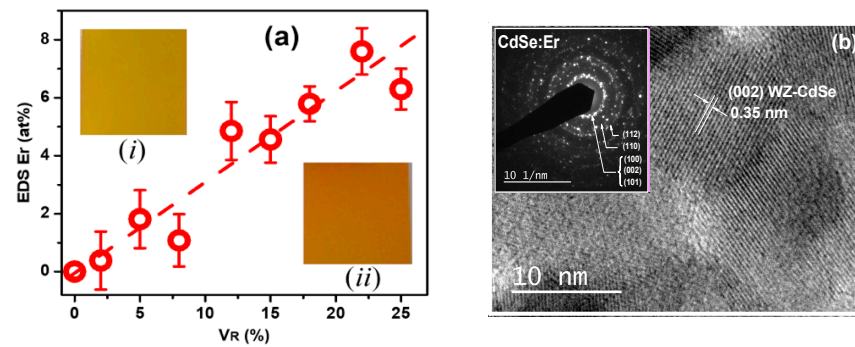


Figure 1. (a) EDS as a function of V_R . Dashed line represents a linear fitting. (i) and (ii) insets illustrate images of the $V_R = 15\%$ doped and undoped $\text{Cd}_{1-x}\text{Er}_x\text{S}$ samples, respectively. (b) TEM image of sample for $x = 4.6$ at%, where the (002) planes of wurtzite phase of CdSe are represented. The inset shows a SAED pattern of the WZ crystalline structure.

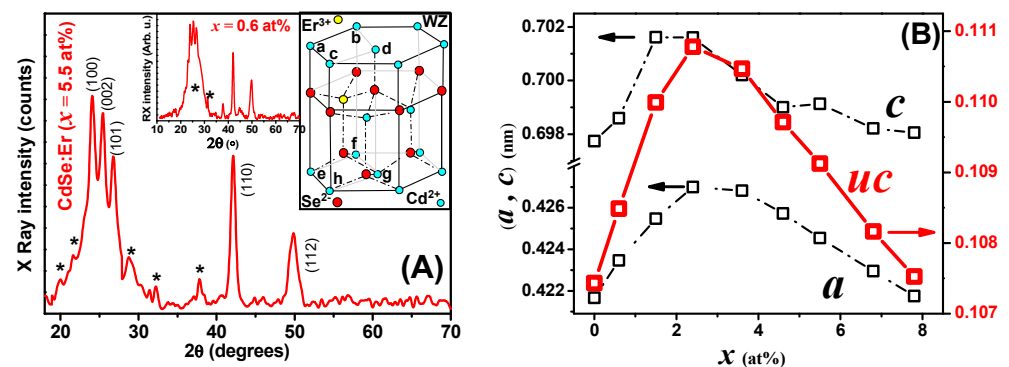


Figure 2. (A) XRD pattern of the CdSe:Er film for $x = 5.5$ at%. The left inset shows the pattern for $x = 0.6$ at%. The right inset illustrates the unit cell of WZ-CdSe lattice. (B) (left axis) lattice parameters a and c versus x , (right axis) primitive unit cell volume versus x .

The size of the CdSe:Er nanoparticles, observed by HRTEM coincides with the size of the crystallites observed by XRD [52]. In our case, the sizes of the crystallite (determined by XRD) using the Monshi–Scherrer equation [53] are comparable to the size of the particle sizes (observed by TEM). The observed nanoparticles are in the 8–15 nm size range (Figure 1b).

The XRD patterns revealed the CdSe and Er_2O_3 phases of the doped films and the right inset in Figure 2A shows the hexagonal WZ unit cell (UC) of CdSe, where the yellow circle represents the Er^{3+} ion in a Cd^{2+} site. The ab.gh parallelepiped represents the primitive UC with side “ a ” and height “ c ”, which correspond to the WZ lattice parameters. Figure 2B on the other hand, displays the a and c values of the UC as a function of the doping level, x . The corresponding data in the left axis reveals that for both parameters, there is an initial increasing tendency that reaches a maximum at around $x \sim 2.4$ at%, and that is followed by a decreasing trend. As expected, the UC volume (right axis graph) follows a similar volcano shaped curve.

It is evident from the XRD pattern’s peaks that all films are polycrystalline, as well as from the spreading diffraction peak and the small shift in the (002) crystal plane. The integration of the Er^{3+} ion into the crystal structure of the CdSe film causes a shift in this peak that rises with Er^{3+} . The (100) and (002) planes are positioned in the CdSe:Er film’s

strongest reflection peaks. We believe that this behavior is related to Er^{3+} ion inclusion in the crystal lattice, which results in preferred orientation in certain crystal planes. The size of the ionic radii of Er^{3+} should be related with the lowest energy that favors preferential orientation in these crystal planes. The WZ phase is indicated by strong peaks on the CdSe:Er film, which indicates a better crystallinity.

The interesting relationship of the UC dimension data and the doping level of the semiconductor material can be interpreted considering the work of Hsu et al. [54] who reported a study of Er:GaSe. These authors suggested that the two acceptor levels were originated either from the substitution (SBSs) of one Er^{3+} for one pair of Ga^{2+} or interstitial (INs) insertion of one Er^{3+} at interlayer sites. In the case of the material under study, it is possible to note that since the ionic radii are Cd^{2+} : 0.95 Å, Er^{3+} : 0.89 Å and Se^{2-} : 2.025 Å, we can assume that Er^{3+} ions occupy Cd^{2+} sites (similar cation-size). However, with a further increase in the Er dopant concentration, the dopant ions are probably incorporated at the interstitial sites (several papers have reported this change) [55–59]. Based on this, it is possible to suggest that according to the oxidation state of the Er^{3+} ion, this chemical species is incorporated into the crystal lattice of CdSe replacing a Cd^{2+} ion, thus providing an extra hole due to its deficiency in valence electrons (similar investigations have been reported for CdSe:Er films) [60].

Raman spectra of Er-doped CdSe nanocrystalline thin films in 150–700 cm^{-1} intervals can be seen in Figure 3a. An inspection of the corresponding data shows an increase in the phonon signals as x increases. These observations are similar to those reported by Portillo et al. [60]. A Raman spectrum of a representative CdSe:Er sample is exhibited in Figure 3a, where three overtones are observed in addition to the optical longitudinal A1LO mode at 205 cm^{-1} of the WZ CdSe structure. A Raman phonon mode for the monoclinic structure of Er_2O_3 at ~560 cm^{-1} can also be seen in the CdSe:Er spectrum of Figure 3b [61]. The 1LO phonon mode shows an asymmetric band, which reflects the presence of a surface mode [62]. In nanocrystals (NCs) this is mainly due to a high surface to volume ratio [63], surface-ions-bond contraction and quantum confinement [64]. Deconvolution of these signals separates the 1LO and the surface phonon modes (SPM), A and B, as shown in the inset of Figure 3c. The lower inset shows the 1LO mode in a magnified scale, where the frequency position as a function of x is clearly observed. This relationship resembles an inverse function of the CdSe UC versus x (see Figure 2B), in which lattice expansion implies phonon softening, and lattice contraction and phonon hardening. In the inset of Figure 3c on the other hand, it is possible to observe vibration displacements of the 1LO mode, which reflect bond-stretching vibrations [65]. As it was previously indicated, contraction or expansion of the CdSe lattice depends on the concentration of Er^{3+} impurities in the interstitial sites of the CdSe lattice. The B-data trend in Figure 3c indicates that the SPM shifts to lower frequencies when the doping increases; a fact that suggests that disorder augments almost monotonically as x increases [66,67].

Figure 4a shows the Tauc method data used to calculate the CdSe direct energy band gap, E_g , in which the $(\alpha h\nu)^2$ versus $h\nu$ plot was employed [68]. Here, α is the optical absorption coefficient, which was determined from the optical transmittance (T_o) ($\alpha = [\text{Log}\{100/T_o\}]/[\tau \text{Log}e]$), $h\nu$ is the photon energy; and only four samples are exhibited for clarity. The inset in this figure shows T_o spectra for the same four samples chosen for E_g calculation. Figure 4b displays E_g as function of x for the entire $0.0 \leq x \leq 7.8$ at% range. The E_g dependence on x is in agreement with the UC vs. x plot, because, in general, if UC increases, E_g is reduced, and vice versa. However, this is not in agreement with the average crystal size (ACS) as function of x , since it can be readily seen that as ACS decreases, E_g also decreases. This is contrary to the quantum confinement effect since ACS should be within the strong quantum confinement regime (CdSe Bohr radius: 5.3 nm) [69]. This anomalous behavior can be explained considering the modifications in the lattice produced by the doping, which in turn can result in distortion, vacancies, interstitials, stress, expansion, contraction and non-stoichiometry effects, which can break the crystal symmetry and modify the physical properties of materials [70–73], particularly

in the case of lanthanide doping [74]. The ACS dependence on x can be explained by surface tension increase that reduces crystal size when Er^{3+} bonds at the NC surface are formed [75,76]. It is also interesting to note that at $x \cong 4.6$ at%, the effect of Er^{3+} on the NCs volume becomes important, and the ACS starts to increase. It can also be observed that the crystal size (Figure 4b green) behaves inversely to the unit cell size (Figure 2B red). We have obtained different values of E_g shown in Figure 4b red. E_g decreases with increasing erbium doping up to $x = 4.6\%$, then it increases for $x = 5.5$ to 7.8% . The decrease in E_g may be due to the erbium electron localized states that create new states near the conduction band, leading to a reduction in the band gap of pure CdSe (similar observations were reported for ZnO) [77]. The variation in band gap depends also on particle size (Figure 4b green) and lattice parameters (Figure 2B). The decrease in particle size with increasing doping concentration leads to a rising of the band gap as the quantum refinement effect occurs [78]. The Bras' effective mass model [79] can also explain our results. The energy gap (E_g) of the nanoparticles can be expressed, according to Bras' effective mass model, as a function of particle size, as shown by the following expression:

$$E_g = E_{bulk} + \frac{\hbar^2 \pi^2}{2R^2} \left[\frac{1}{m_e} + \frac{1}{m_h} \right] - \frac{1.8e^2}{\epsilon R} \quad (1)$$

where E_g is the measured band gap of the nanoparticles, E_{bulk} is the band gap of the bulk semiconductor, \hbar is the second Plank's constant, R is the radius of the nanoparticle, m_e is the effective mass of the electron, m_h is the effective mass of the hole, e is the charge of electron, and ϵ is the electric permittivity of the material. The lattice parameters (a and c) and the unit cell volume (V) of nanoparticles can be calculated with the following equation:

$$\frac{1}{d^2} = \frac{4}{3} \left(\frac{h^2 + hk + k^2}{a^2} \right) + \frac{l^2}{c^2} \quad (2)$$

$$V = \frac{\sqrt{3}}{2} a^2 c \quad (3)$$

where d is the interplanar distance and (h, k, l) are the Miller indices. The ratio a, c and the unit cell volume (V) for pure and Er-doped samples are shown in Figure 2B. It can be noticed that a, c and V are affected by erbium doping with an increase in their values up to $x = 2.4\%$ with respect to the pure sample. This behavior of a, c and V may be attributed to changes in the ionic size of Er^{3+} (0.89\AA) substituting Cd^{2+} (0.95\AA) in CdSe lattice. a, c and V decrease for $x > 2.4\%$ and in the end, they approach the values of pure CdSe. This cell contraction may be explained by the larger Er^{3+} ions leaving the CdSe lattice at high doping concentrations ($x > 2.4\%$) to form the Er_2O_3 impurity [80,81]. The decrease in the lattice parameter c may also be attributed to the formation of defects in the CdSe lattice as a result of increasing the number of dopant (Er^{3+}) ions, Dakhel et al. reported similar behavior when performing a different doping experiment [82].

Figure 5a shows the dark d.c. conductivity (σ) dependences (presented on a semi-logarithmic scale) of $\text{Cd}_{1-x}\text{Er}_x\text{Se}$, in the 10^{-7} to $10^1 \Omega^{-1} \text{cm}^{-1}$ range, versus the inverse of the absolute temperature (T) times k ($1/kT$). Here, k corresponds to the Boltzmann constant. A metallic behavior of $\log(\sigma)$ vs. $1/kT$ is observed for $x = 0.6, 1.5$ and 2.4 at%, since σ remains essentially constant in the $300 \geq T \geq 35$ K range (which is $35 \leq 1/kT \leq 110$ (eV) $^{-1}$), and decreases for $T \leq 35$ K. For $3.6 \leq x \leq 7.8$ at%, the behavior is that of a semiconductor with shallow donor levels, where the free carrier density decreases as x increases. The metallic dependence of $\log(\sigma)$ vs. T has been observed in ITO films grown by reactive plasma [83], and has been attributed to disorder in the lattice. Grenberg and coworkers [84] also reported a similar behavior at low temperatures for ZnO nanocrystals (NCs), which was obtained by changing the contact area and the center-to-center distance between NCs. A strong decrease in free carriers' lifetime has been reported when the Er concentration increases, due to the formation of NCs [85,86].

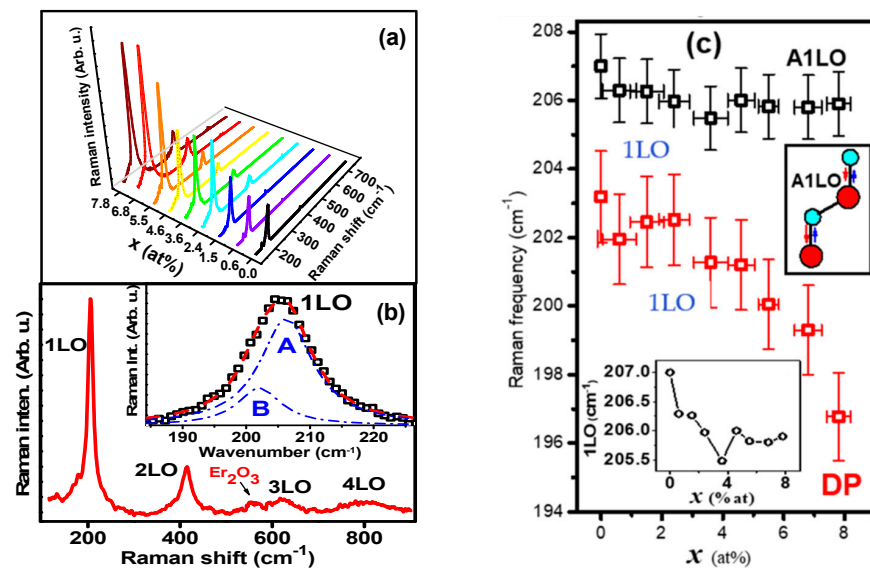


Figure 3. (a) Phonon Raman spectra of the series of $\text{Cd}_{1-x}\text{Er}_x\text{Se}$ samples. (b) Raman spectrum of a representative CdSe:Er sample where the 1LO phonon mode and up to the third overtone are observed, a Raman signal from Er_2O_3 is revealed in the spectrum. The inset illustrates the deconvolution of the band at $\sim 205\text{ cm}^{-1}$ in the 1LO mode (A) and the surface mode (B). (c) The 1LO (A) and the surface (B) modes positions against x . The low inset exhibits the 1LO mode position vs. x in a magnified scale. The right inset illustrates the A1LO mode oscillation.

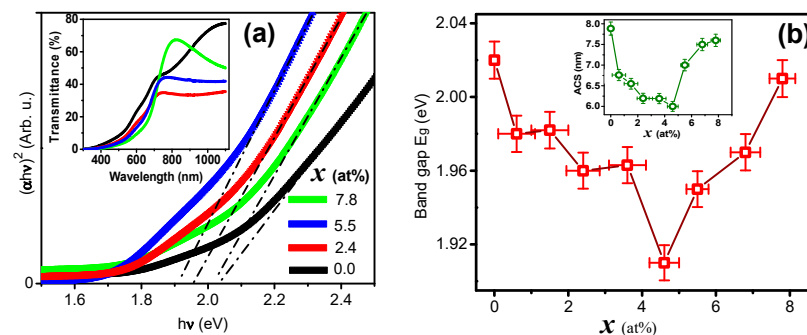


Figure 4. (a) Tauc method to calculate the direct energy band gap (E_g) of the $\text{Cd}_{1-x}\text{Er}_x\text{Se}$ for four values of x . The inset illustrates the optical transmittance (T_o) spectra for the same samples chosen for E_g calculation. (b) Direct band gap as function of x , the inset depicts the average crystal size (ACS) versus x plot.

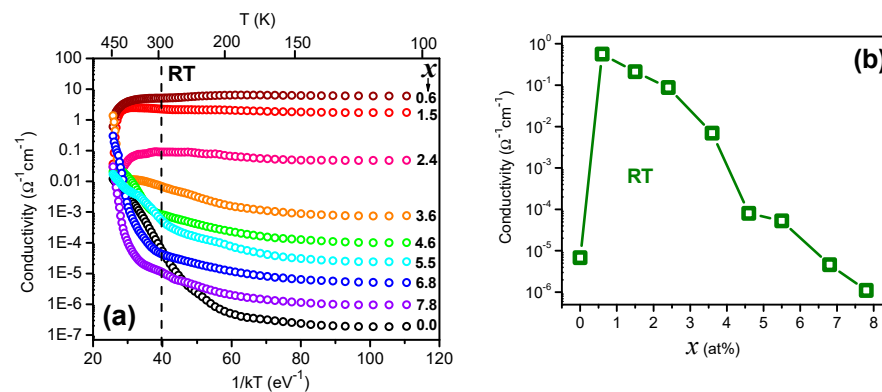


Figure 5. (a) Dark d.c. conductivity (σ) vs. inverse of absolute temperature (T). (b) Room temperature (RT) dark d.c. conductivity σ as a function of x .

In the case of the CdSe:Er NCs of this work, the incorporation of Er³⁺ produces an effective doping at low Er concentrations. When x rises, the formation of Er₂O₃ NCs (previously observed in XRD and Raman analysis) can produce barriers between the CdSe NCs which scatter the free carriers that, in turn, generate non-radiative transitions. σ at RT versus x is displayed in Figure 5b (see also dotted line in Figure 5a). The corresponding plot reveals that for low x values, σ increases almost five orders of magnitude. When Er concentration increases up to $x = 7.8$ at%, σ diminishes to values lower than those of the undoped sample. In this context, doping ZnO with Er³⁺ [87] and Ho³⁺ [88] shows that σ decreases when the impurity concentration increases. In the first case, the decrease is attributed to impurities scattering of free carriers and in the second case, to trapping at grain boundaries. Another effect of the Er³⁺ ion incorporation is the decrease in the crystallite size, which leads to higher grain boundary scattering, decreasing the mobility as well as the conductivity. As described by Callaway, when the grain size is decreased, the scattering rate of phonons become higher. Hence, it will lower the value of conductivity, which is favorable for various materials. However, as conductivity is reduced, the value of grain boundary scattering increases [89]. Morais et al., in their experiment of Er doped SnO₂ thin films, indicate that by analogy, the overall effect of increasing the Er concentration is to decrease the film conductivity since an increase in the electric charge compensation, and decrease in the crystallite size, result in a decrease in the mobility since the grain boundary scattering is increased [90].

Photoluminescence (PL) measurements on the materials under study were carried out using as excitation source the 2.808 eV (441.6 nm) line of a He-Cd laser. Figure 6a displays the spectra for the Cd_{1-x}Er_xSe films registered for all the films in the $0.0 \leq x \leq 7.8$ at% range. All the samples exhibit a single PL broad band in the 1.4–2.5 eV interval (496–886 nm). Very narrow PL signals from Er³⁺ intra-atomic transitions [91] are observed in all spectra except for the undoped sample ($x = 0$). Several authors [92,93] report PL emission of rare earths doped and undoped CdSe NCs with a broad band centered in the 2.06–2.25 eV (550–600 nm) interval. The CdSe:Er samples of this work show the same PL band whose position depends on the NC size, doping type, and crystal defects. Other than the Er intra-atomic level transitions, no PL signals from Er₂O₃ oxide (see Figure 2A) could be observed. Figure 6b exhibits the PL band position (PLBP) as a function of the doping level x . Inspection of this data reveals that PLBP decreases in the $0.0 \leq x \leq 4$ at% interval and increases for the remaining values. PLPB follows a tendency similar to that of the band gap (see Figure 4b), since PLBP is defined by an exciton emission [93]. The PLBP intensity versus x plot (right axis) does not show a gradual increase in the intensity. This result is not clear. It seems that PL intensity emission is reduced for smaller NPs and increases for larger sizes (see inset of inset of Figure 4b). As it was previously indicated, the crystalline quality of CdSe:Er films improves as x increases; a fact that suggests that defects on the NCs surface are responsible for the intensity abatement of PL spectra. The non-radiative transitions at the surface are increased when NC size decreases, along the $0.0 \leq x \leq 4.6$ at% interval (see inset of Figure 4b). It is interesting note that a strong decrease in PL emissions has been observed in Er-doped GaAs due to the presence of ErAs precipitates in the GaAs matrix; giving place to Schottky barriers at the Er₂O₃-GaAs interface, which in turn form high n- and p-type depletion regions of high resistivity and very short carrier lifetimes [86]. Doping Er³⁺ in Hf-Al-silicate forms Er₂O₃ close the surface of planar waveguides, where the carriers' lifetime decreases when the Er concentration increases [85]. In the case of the CdSe:Er samples under study, while lifetime and PL decreases for low Er concentrations, NC increases for higher x values ($x \sim 4.6$ at%) where radiative transitions surpass non-radiative ones because the surface/volume ratio increases. As a consequence, the carriers' lifetime also increases [94]. High density of Er₂O₃ NCs on the other hand, reduces σ and enhances PL signals.

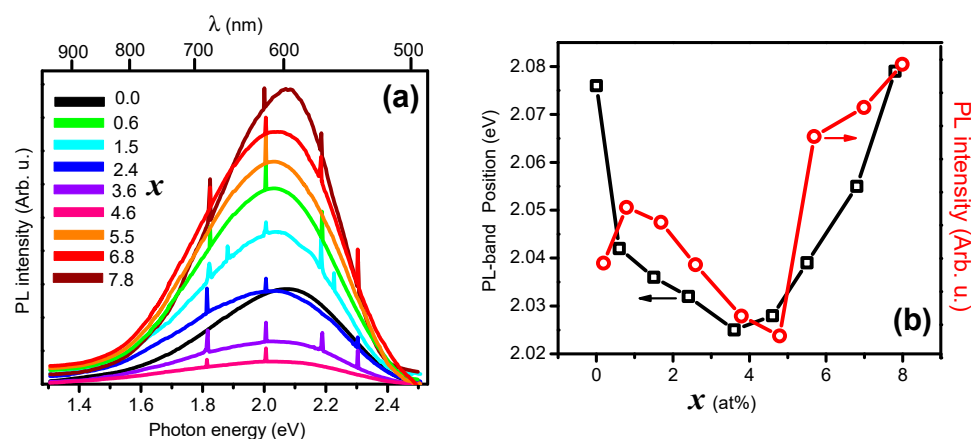


Figure 6. (a) Photoluminescence spectra of all the set of $\text{Cd}_{1-x}\text{Er}_x\text{Se}$ samples. (b) Energy position of the PL band maximum (left axis) and PL band intensity (right axis) versus x .

4. Conclusions

In summary, Er incorporation in CdSe nanocrystals provokes drastic changes in the $\text{Cd}_{1-x}\text{Er}_x\text{Se}$ lattice structure, depending on the level of Er doping. For low x values, Er^{3+} ions are sequentially incorporated as follows: (i) replacement of Cd^{2+} ions, (ii) to interstitial sites, and (iii) to NCs surface. In the first (i) case, the unit cell volume tends to increase, and in the (ii) and (iii) cases, it tends to decrease. Er^{3+} in Cd^{2+} sites induce crystalline quality of CdSe as suggested from XRD and Raman measurements, thus Er^{3+} reduces the structural disorder but increases the chemical one. When the lattice expands, the 1LO phonon softens, and as expected, hardens if the lattice contracts. The surface mode softens continuously when x increases, which indicates that chemical disorder increases. The CdSe energy band gap decreases when UC increases and increases in the opposite case, which is a property of all semiconductors. Er_2O_3 NCs grow as a secondary phase, which forms barriers at the oxide-semiconductor interface, which gradually reduces the carriers transfer through the interface when x increases and, consequently, the film dark conductivity decreases. On the other hand, the Er_2O_3 -CdSe band gap coupling enhances the photoluminescence, via conversion in the oxide, of CdSe. The findings of this work can be useful for the design of CdSe-based devices.

Author Contributions: Y.d.J.A.-S.: experimental, investigation, methodology, formal analysis; L.A.G.: formal analysis, resources; M.T.-A.: investigation, formal analysis; R.L.-M.: resources, validation; O.Z.-A.: Validation, Writing; A.M.-L.: Validation, visualization, Writing—Review & Editing. All authors have read and agreed to the published version of the manuscript.

Funding: This research received no external funding.

Institutional Review Board Statement: Not applicable.

Informed Consent Statement: Not applicable.

Data Availability Statement: The datasets used and/or analyzed during the current study are available from the corresponding author on reasonable request.

Conflicts of Interest: The authors declare no conflict of interest.

References

1. Babu, N.S.; Khadar, M.A. Electrical properties of grain size tuned CdSe nanocrystal films for practical applications. *Sol. Energy Mater. Sol. Cells* **2018**, *178*, 106–114. [[CrossRef](#)]
2. Hassen, M.; Riahi, R.; Laatar, F.; Ezzaouia, H. Optical and surface properties of CdSe thin films prepared by sol-gel spin coating method. *Surf. Interfaces* **2019**, *18*, 100408. [[CrossRef](#)]
3. Ghobadi, N.; Sohrabi, P.; Hatami, H.R. Correlation between the photocatalytic activity of CdSe nanostructured thin films with optical band gap and Urbach energy. *Chem. Phys.* **2020**, *538*, 110911. [[CrossRef](#)]

4. Dai, G.; Chen, Y.; Wan, Q.; Zhang, Q.; Pan, A.; Zou, B. Fabrication and optical waveguide of Sn-catalyzed CdSe microstructures. *Solid State Commun.* **2013**, *167*, 31–35. [[CrossRef](#)]
5. Shyju, T.; Anandhi, S.; Indirajith, R.; Gopalakrishnan, R. Solvothermal synthesis, deposition and characterization of cadmium selenide (CdSe) thin films by thermal evaporation technique. *J. Cryst. Growth* **2011**, *337*, 38–45. [[CrossRef](#)]
6. Bayramoglu, H.; Peksoz, A. Electronic energy levels and electrochemical properties of co-electrodeposited CdSe thin films. *Mater. Sci. Semicond. Process.* **2019**, *90*, 13–19. [[CrossRef](#)]
7. Smith, A.M.; Nie, S. Semiconductor Nanocrystals: Structure, Properties, and Band Gap Engineering. *Acc. Chem. Res.* **2010**, *43*, 190–200. [[CrossRef](#)]
8. Sahu, A.; Kang, M.S.; Kompch, A.; Notthoff, C.; Wills, A.W.; Deng, D.; Winterer, M.; Frisbie, C.D.; Norris, D.J. Electronic Impurity Doping in CdSe Nanocrystals. *Nano Lett.* **2012**, *12*, 2587–2594. [[CrossRef](#)]
9. Tolbert, S.H.; Alivisatos, A.P. Size Dependence of a First Order Solid-Solid Phase Transition: The Wurtzite to Rock Salt Transformation in CdSe Nanocrystals. *Science* **1994**, *265*, 373–376. [[CrossRef](#)]
10. Trallero-Giner, C.; Debernardi, A.; Cardona, M.; Proupin, E.M.; Ekimov, A.I. Optical vibrons in CdSe dots and dispersion relation of the bulk material. *Phys. Rev. B* **1998**, *57*, 4664–4669. [[CrossRef](#)]
11. Delikanli, S.; Yu, G.; Yeltik, A.; Bose, S.; Erdem, T.; Yu, J.; Erdem, O.; Sharma, M.; Sharma, V.; Quliyeva, U.; et al. Ultrathin Highly Luminescent Two-Monolayer Colloidal CdSe Nanoplatelets. *Adv. Funct. Mater.* **2019**, *29*, 1901028. [[CrossRef](#)]
12. Alasvand, A.; Kafashan, H. Comprehensive physical studies on nanostructured Zn-doped CdSe thin films. *J. Alloys Compd.* **2019**, *789*, 108–118. [[CrossRef](#)]
13. Garg, N. A Brief Study on Characteristics, Properties, and Applications of CdSe. *Proc. ICEMIT* **2017**, *2*, 43–60.
14. Yu, J.; Chen, R. Optical properties and applications of two-dimensional CdSe nanoplatelets. *Infomat* **2020**, *2*, 905–927. [[CrossRef](#)]
15. Zhao, L.; Hu, L.; Fang, X. Growth and Device Application of CdSe Nanostructures. *Adv. Funct. Mater.* **2012**, *22*, 1551–1566. [[CrossRef](#)]
16. Trindade, T.; O'Brien, P.; Zhang, X.-M. Synthesis of CdS and CdSe Nanocrystallites Using a Novel Single-Molecule Precursors Approach. *Chem. Mater.* **1997**, *9*, 523–530. [[CrossRef](#)]
17. Ahmed, M.; Guleria, A.; Rath, M.C.; Singh, A.K.; Adhikari, S.; Sarkar, S.K. Facile and green synthesis of CdSe quantum dots in protein matrix: Tuning of morphology and optical properties. *J. Nanosci. Nanotechnol.* **2014**, *14*, 5730–5742. [[CrossRef](#)] [[PubMed](#)]
18. Xi, L.; Lam, Y.M.; Xu, Y.P.; Li, L.-J. Synthesis and characterization of one-dimensional CdSe by a novel reverse micelle assisted hydrothermal method. *J. Colloid Interface Sci.* **2008**, *320*, 491–500. [[CrossRef](#)]
19. Thomas, D.; Lee, H.O.; Santiago, K.C.; Pelzer, M.; Kuti, A.; Jenrette, E.; Bahoura, M. Rapid Microwave Synthesis of Tunable Cadmium Selenide (CdSe) Quantum Dots for Optoelectronic Applications. *J. Nanomater.* **2020**, *2020*, 5056875. [[CrossRef](#)]
20. Skaff, H.; Emrick, T. Reversible Addition Fragmentation Chain Transfer (RAFT) Polymerization from Unprotected Cadmium Selenide Nanoparticles. *Angew. Chem. Int. Ed.* **2004**, *43*, 5383–5386. [[CrossRef](#)]
21. Li, J.; Hao, X.; Wang, J.; Cui, X.; Li, X.; Wei, S.; Lu, J. Layered Inorganic/Organic Hybrid (CdSe) n-Monoamine Nanobelts: Controllable Solvothermal Synthesis, Multiple Stage Amine De-Intercalation Transformation, and Two-Dimensional Exciton Quantum Confinement Effect. *Inorg. Chem.* **2018**, *57*, 10781–10790. [[CrossRef](#)]
22. Miethe, J.F.; Schlosser, J.A.; Eckert, G.; Lübke, F.; Bigall, N.C. Electronic transport in CdSe-polymer fibres. *J. Mater. Chem. C* **2018**, *6*, 10916–10923. [[CrossRef](#)]
23. Yildiz, I.; Callan, B.; Cruickshank, S.F.; Callan, J.F. Biocompatible CdSe-ZnS Core-Shell Quantum Dots Coated with Hydrophilic Polythiols. *Langmuir* **2009**, *25*, 7090–7096. [[CrossRef](#)]
24. Huang, C.; Mao, J.; Chen, X.M.; Yang, J.; Du, X.W. Laser-activated gold catalysts for liquid-phase growth of cadmium selenide nanowires. *Chem. Commun.* **2014**, *51*, 2145–2148. [[CrossRef](#)] [[PubMed](#)]
25. Rajan, P.I.; Vijaya, J.J.; Jesudoss, S.K.; Kaviyarasu, K.; Lee, S.-C.; Kennedy, L.J.; Jothiramingam, R.; Al-Lohedan, H.A.; Abdullah, M.M. Investigation on preferably oriented abnormal growth of CdSe nanorods along (0002) plane synthesized by henna leaf extract-mediated green synthesis. *R. Soc. Open Sci.* **2018**, *5*, 171430. [[CrossRef](#)] [[PubMed](#)]
26. Bonilla, J.C.; Bozkurt, F.; Ansari, S.; Sozer, N.; Kokini, J.L. Applications of quantum dots in Food Science and biology. *Trends Food Sci. Technol.* **2016**, *53*, 75–89. [[CrossRef](#)]
27. Almeida-Silva, A.C.; Peres-Freschi, A.P.; Mendonça-Rodrigues, C.; França-Matias, B.; Prado-Maia, L.; Goulart, L.R.; Oliveira-Dantas, N. Biological analysis and imaging applications of CdSe/Cd_xSe_{1-x}/CdS core-shell magic-sized quantum dot. *Nanomed. Nanotechnol. Biol. Med.* **2016**, *12*, 1421–1430. [[CrossRef](#)]
28. Ung, T.D.T.; Tran, T.K.C.; Pham, T.N.; Nguyen, D.N.; Dinh, D.K.; Nguyen, Q.L. CdTe and CdSe quantum dots: Synthesis, characterizations and applications in agriculture. *Adv. Nat. Sci. Nanosci. Nanotechnol.* **2012**, *3*, 043001. [[CrossRef](#)]
29. Duppall, R.; Nejo, A.A.; Pullabhotla, V.S.R.; Opoku, A.R.; Revaprasadu, N.; Shonhai, A. An In Vitro Assessment of the Interaction of Cadmium Selenide Quantum Dots With DNA, Iron, and Blood Platelets. *IUBMB Life* **2012**, *64*, 995–1002. [[CrossRef](#)]
30. Sathyalatha, K.; Uthanna, S.; Reddy, P. Electrical and photoconducting properties of vacuum evaporated pure and silver-doped CdSe films. *Thin Solid Films* **1989**, *174*, 233–238. [[CrossRef](#)]
31. Walukiewicz, W. Intrinsic limitations to the doping of wide-gap semiconductors. *Phys. B Condens. Matter* **2001**, *302–303*, 123–134. [[CrossRef](#)]
32. Majid, A.; Arshad, H.; Murtaza, S. Synthesis and characterization of Cr doped CdSe nanoparticles. *Superlattices Microstruct.* **2015**, *85*, 620–623. [[CrossRef](#)]

33. Whitham, P.J.; Knowles, K.E.; Reid, P.J.; Gamelin, D.R. Photoluminescence Blinking and Reversible Electron Trapping in Copper-Doped CdSe Nanocrystals. *Nano Lett.* **2015**, *15*, 4045–4051. [[CrossRef](#)] [[PubMed](#)]
34. Proshchenko, V.; Dahnovsky, Y. Magnetic effects in Mn-doped CdSe nanocrystals. *Phys. Status Solidi B* **2015**, *252*, 2275–2279. [[CrossRef](#)]
35. Al-Kabbi, A.S.; Sharma, K.; Saini, G.; Tripathi, S. Effect of doping on transport properties of nanocrystalline CdSe thin film. *Thin Solid Films* **2015**, *586*, 1–7. [[CrossRef](#)]
36. Sharma, K.; Al-Kabbi, A.S.; Saini, G.; Tripathi, S. Influence of Zn doping on structural, optical and electrical properties of nanocrystalline CdSe thin films. *J. Alloys Compd.* **2015**, *651*, 42–48. [[CrossRef](#)]
37. Zhang, K.-C.; Li, Y.-F.; Liu, Y.; Chi, F. Density-functional study on the robust ferromagnetism in rare-earth element Yb-doped SnO₂. *J. Magn. Magn. Mater.* **2014**, *360*, 165–168. [[CrossRef](#)]
38. Lee, W.; Kwak, W.-C.; Min, S.K.; Lee, J.-C.; Chae, W.-S.; Sung, Y.-M.; Han, S.-H. Spectral broadening in quantum dots-sensitized photoelectrochemical solar cells based on CdSe and Mg-doped CdSe nanocrystals. *Electrochem. Commun.* **2008**, *10*, 1699–1702. [[CrossRef](#)]
39. Martín-Rodríguez, R.; Geitenbeek, R.; Meijerink, A. Incorporation and Luminescence of Yb³⁺ in CdSe Nanocrystals. *J. Am. Chem. Soc.* **2013**, *135*, 13668–13671. [[CrossRef](#)]
40. Li, I.-F.; Yeh, C.-S. Synthesis of Gd doped CdSe nanoparticles for potential optical and MR imaging applications. *J. Mater. Chem.* **2010**, *20*, 2079–2081. [[CrossRef](#)]
41. Hanifehpour, Y.; Joo, S.W. Synthesis, characterization and sonophotocatalytic degradation of an azo dye on Europium doped cadmium selenide nanoparticles. *Nanochemistry Res.* **2018**, *3*, 178–188.
42. Tomás, S.A.; Lozada-Morales, R.; Portillo, O.; Lima-Lima, H.; Palomino-Merino, R.; Zelaya, O. Characterization of chemical bath deposited CdS thin films doped with methylene blue and Er³⁺. *Eur. Phys. J. Spéc. Top.* **2008**, *153*, 299–302. [[CrossRef](#)]
43. Moreno, O.P.; Pérez, R.G.; Portillo, M.C.; Téllez, G.H.; Rosas, E.R.; Cruz, S.C.A. Moreno Rodríguez, Synthesis, morphological, optical and structural properties of PbSSe₂–nanocrystals. *Optik* **2016**, *127*, 8341–8349. [[CrossRef](#)]
44. Dammak, M.; Zhang, D.-L. Spectra and energy levels of Er³⁺ in Er₂O₃ powder. *J. Alloys Compd.* **2006**, *407*, 8–15. [[CrossRef](#)]
45. Al-Kuhaili, M.F.; Durrani, S.M.A. Optical properties of erbium oxide thin films deposited by electron beam evaporation. *Thin Solid Films* **2007**, *515*, 2885–2890. [[CrossRef](#)]
46. Ionescu, A.M.; Munteanu, D.; Chovet, A.; Rusu, A.; Steriu, D. The intrinsic pseudo-MOSFET technique. In Proceedings of the 1997 International Semiconductor Conference 20th Edition, Sinaia, Romania, 7–11 October 1997; Volume 1, pp. 217–220.
47. Bakhsh, A.; Maqsood, A. Sintering effects on structure, morphology, and electrical properties of sol-gel synthesized, nanocrystalline erbium oxide. *Electron. Mater. Lett.* **2012**, *8*, 605–608. [[CrossRef](#)]
48. Bhatia, S.; Verma, N. Erbium-doped nanoparticles/films for enhancing percentage photodegradation of direct red-31 dye. *J. Mater. Sci. Mater. Electron.* **2018**, *29*, 14960–14970. [[CrossRef](#)]
49. Hegazy, M.A.; El-Hameed, A.M. A Characterization of CdSe-nanocrystals used in semiconductors for aerospace applications: Production and optical properties. *NRIAG J. Astron. Geophys.* **2014**, *3*, 82–87. [[CrossRef](#)]
50. Alajlouni, S.; Sun, Z.Y.; Li, J.; Zavada, J.M.; Lin, J.Y.; Jiang, H.X. Refractive index of erbium doped GaN thin films. *Appl. Phys. Lett.* **2014**, *105*, 081104. [[CrossRef](#)]
51. Kenyon, A.J. Erbium in silicon. *Semicond. Sci. Technol.* **2005**, *20*, R65–R84. [[CrossRef](#)]
52. Yu, J.; Zhang, C.; Pang, G.; Sun, X.W.; Chen, R. Effect of Lateral Size and Surface Passivation on the Near-Band-Edge Excitonic Emission from Quasi-Two-Dimensional CdSe Nanoplatelets. *ACS Appl. Mater. Interfaces* **2019**, *11*, 41821–41827. [[CrossRef](#)]
53. Nasiri, S.; Hosseinneshad, M.; Rabiei, M.; Palevicius, A.; Janusas, G. The effect of calcination temperature on the photophysical and mechanical properties of copper iodide (5 mol%)-doped hydroxyapatite. *Opt. Mater.* **2021**, *121*, 111559. [[CrossRef](#)]
54. Hsu, Y.-K.; Chen, C.-W.; Huang, J.Y.; Pan, C.-L.; Zhang, J.-Y.; Chang, C.-S. Erbium doped GaSe crystal for mid-IR applications. *Opt. Express* **2006**, *14*, 5484–5491. [[CrossRef](#)] [[PubMed](#)]
55. Chen, X.; Shangguan, W. Hydrogen production from water splitting on CdS-based photocatalysts using solar light. *Front. Energy* **2013**, *7*, 111–118. [[CrossRef](#)]
56. Cheng, L.; Xiang, Q.; Liao, Y.; Zhang, H. CdS-Based photocatalysts. *Energy Environ. Sci.* **2018**, *11*, 1362–1391. [[CrossRef](#)]
57. Su, J.; Zhang, T.; Li, Y.; Chen, Y.; Liu, M. Photocatalytic Activities of Copper Doped Cadmium Sulfide Microspheres Prepared by a Facile Ultrasonic Spray-Pyrolysis Method. *Molecules* **2016**, *21*, 735. [[CrossRef](#)]
58. Liu, M.; Du, Y.; Ma, L.; Jing, D.; Guo, L. Manganese doped cadmium sulfide nanocrystal for hydrogen production from water under visible light. *Int. J. Hydrogen Energy* **2012**, *37*, 730–736. [[CrossRef](#)]
59. Wang, H.; Chen, W.; Zhang, J.; Huang, C.; Mao, L. Nickel nanoparticles modified CdS—A potential photocatalyst for hydrogen production through water splitting under visible light irradiation. *Int. J. Hydrogen Energy* **2015**, *40*, 340–345. [[CrossRef](#)]
60. Portillo-Moreno, O.; Gutiérrez-Pérez, R.; Palomino-Merino, R.; Chávez-Portillo, M.; Márquez-Specia, M.N.; Hernández-Torres, M.E.; Gracia-Jiménez, M.; Cerna, J.R.; Zamora-Tototzintle, M. Near-infrared-to-visible upconverting luminescence of Er³⁺-doped CdSe nanocrystals grown by chemical bath. *Optik* **2017**, *138*, 229–239. [[CrossRef](#)]
61. Yan, D.; Wu, P.; Zhang, S.P.; Liang, L.; Yang, F.; Pei, Y.L.; Chen, S. Assignments of the Raman modes of monoclinic erbium oxide. *J. Appl. Phys.* **2013**, *114*, 193502. [[CrossRef](#)]
62. Ferrari, A.C. Raman spectroscopy of graphene and graphite: Disorder, electron–phonon coupling, doping and nonadiabatic effects. *Solid State Commun.* **2007**, *143*, 47–57. [[CrossRef](#)]

63. Lin, C.; Kelley, D.F.; Rico, M.; Kelley, A.M. The “Surface Optical” Phonon in CdSe Nanocrystals. *ACS Nano* **2014**, *8*, 3928–3938. [[CrossRef](#)] [[PubMed](#)]
64. Gomonnai, A.V.; Azhniuk, Y.M.; Yukhymchuk, V.O.; Kranjčec, M.; Lopushansky, V.V. Confinement-, surface- and disorder-related effects in the resonant Raman spectra of nanometric $\text{CdS}_{1-x}\text{Se}_x$ crystals. *Phys. Status Solidi B* **2003**, *239*, 490–499. [[CrossRef](#)]
65. Dzhagan, V.; Lokteva, I.; Himcinschi, C.; Jin, X.; Kolny-Olesiak, J.; Zahn, D.R.T. Phonon Raman spectra of colloidal CdTe nanocrystals: Effect of size, non-stoichiometry and ligand exchange. *Nanoscale Res. Lett.* **2011**, *6*, 79. [[CrossRef](#)]
66. Diaz-Reyes, J.; Galvan-Arellano, M.; Mendoza-Alvarez, J.G.; Arias-Ceron, J.S.; Herrera-Perez, J.L.; Lopez-Cruz, E. Characterization of highly doped $\text{Ga}_{0.86}\text{In}_{0.14}\text{As}_{0.13}\text{Sb}_{0.87}$ grown by liquid phase epitaxy. *Rev. Mex. Física* **2017**, *63*, 55–64.
67. Dzhagan, V.M.; Azhniuk, Y.M.; Milekhin, A.G.; Zahn, D.R.T. Vibrational spectroscopy of compound semiconductor nanocrystals. *J. Phys. D Appl. Phys.* **2018**, *51*, 503001. [[CrossRef](#)]
68. Nasiri, S.; Dashti, A.; Hosseinezhad, M.; Rabiei, M.; Palevicius, A.; Doustmohammadi, A.; Janusas, G. Mechanochromic and thermally activated delayed fluorescence dyes obtained from D–A–D’ type, consisted of xanthen and carbazole derivatives as an emitter layer in organic light emitting diodes. *Chem. Eng. J.* **2021**, *430*, 131877. [[CrossRef](#)]
69. Venkatram, N.; Sathyavathi, R.; Rao, D.N. Size dependent multiphoton absorption and refraction of CdSe nanoparticles. *Opt. Express* **2007**, *15*, 12258–12263. [[CrossRef](#)]
70. Gautam, S.K.; Gautam, N.; Singh, R.G.; Ojha, S.; Shukla, D.K.; Singh, F. Anomalous behavior of B_{1g} mode in highly transparent anatase nano-crystalline Nb-doped Titanium Dioxide (NTO) thin films. *AIP Adv.* **2015**, *5*, 127212. [[CrossRef](#)]
71. Choudhury, B.; Choudhury, A. Lattice distortion and corresponding changes in optical properties of CeO_2 nanoparticles on Nd doping. *Curr. Appl. Phys.* **2013**, *13*, 217–223. [[CrossRef](#)]
72. Wang, T.; Layek, A.; Hosein, I.D.; Chirmanov, V.; Radovanovic, P.V. Correlation between native defects and dopants in colloidal lanthanide-doped Ga_2O_3 nanocrystals: A path to enhance functionality and control optical properties. *J. Mater. Chem. C* **2013**, *2*, 3212–3222. [[CrossRef](#)]
73. Sercel, P.C.; Shabaev, A.; Efros, A.L. Photoluminescence Enhancement through Symmetry Breaking Induced by Defects in Nanocrystals. *Nano Lett.* **2017**, *17*, 4820–4830. [[CrossRef](#)] [[PubMed](#)]
74. Zeng, S.; Ren, G.; Xu, C.; Yang, Q. Modifying crystal phase, shape, size, optical and magnetic properties of monodispersed multifunctional NaYbF_4 nanocrystals through lanthanide doping. *CrystEngComm* **2011**, *13*, 4276–4281. [[CrossRef](#)]
75. Bezkravnyi, O.; Małecka, M.A.; Lisiecki, R.; Ostroushko, V.; Thomas, A.G.; Gorantlad, S.; Kepinski, L. The effect of Eu doping on the growth, structure and red-ox activity of ceria nanocubes. *CrystEngComm* **2018**, *20*, 1698–1704. [[CrossRef](#)]
76. Wang, F.; Han, Y.; Lim, C.S.; Lu, Y.; Wang, J.; Xu, J.; Chen, H.; Zhang, C.; Hong, M.; Liu, X. Simultaneous phase and size control of upconversion nanocrystals through lanthanide doping. *Nature* **2010**, *463*, 1061–1065. [[CrossRef](#)] [[PubMed](#)]
77. Anandan, S.; Miyachi, M. Ce-doped ZnO ($\text{Ce}_x\text{Zn}_{1-x}\text{O}$) becomes an efficient visible-light-sensitive photocatalyst by co-catalyst (Cu^{2+}) grafting. *Phys. Chem. Chem. Phys.* **2011**, *13*, 14937–14945. [[CrossRef](#)] [[PubMed](#)]
78. He, H.Y.; Fei, J.; Lu, J. Sm-doping effect on optical and electrical properties of ZnO films. *J. Nanostructure Chem.* **2015**, *5*, 169–175. [[CrossRef](#)]
79. Zhang, F.; Jin, Q.; Chan, S.W. Ceria nanoparticles: Size, size distribution, and shape. *J. Appl. Phys.* **2004**, *95*, 4319–4326. [[CrossRef](#)]
80. Lang, J.; Wang, J.; Zhang, Q.; Xu, S.; Han, D.; Yang, J.; Han, Q.; Yang, L.; Sui, Y.; Li, X.; et al. Synthesis and photoluminescence characterizations of the Er^{3+} -doped ZnO nanosheets with irregular porous microstructure. *Mater. Sci. Semicond. Process.* **2016**, *41*, 32–37. [[CrossRef](#)]
81. Chen, W.-B.; Liu, X.-C.; Li, F.; Chen, H.-M.; Zhou, R.-W.; Shi, E.-W. Influence of oxygen partial pressure on the microstructural and magnetic properties of Er-doped ZnO thin films. *AIP Adv.* **2015**, *5*, 067105. [[CrossRef](#)]
82. Dakhel, A.A.; El-Hilo, M. Ferromagnetic nanocrystalline Gd-doped ZnO powder synthesized by coprecipitation. *J. Appl. Phys.* **2010**, *107*, 123905. [[CrossRef](#)]
83. Shi, J.; Shen, L.; Meng, F.; Liu, Z. Structural, electrical and optical properties of highly crystalline indium tin oxide films fabricated by RPD at room temperature. *Mater. Lett.* **2016**, *182*, 32–35. [[CrossRef](#)]
84. Greenberg, B.L.; Robinson, Z.L.; Ayino, Y.; Held, J.T.; Peterson, T.A.; Mkhoyan, K.A.; Pribiag, V.S.; Aydil, E.S.; Kortshagen, U.R. Metal-insulator transition in a semiconductor nanocrystal network. *Sci. Adv.* **2019**, *5*, eaaw1462. [[CrossRef](#)] [[PubMed](#)]
85. Almeida, R.M.; Marques, A.C.; Cabeça, R.; Zampedri, L.; Chiasera, A.; Ferrari, M. Photoluminescence of Erbium-Doped Silicate Sol-Gel Planar Waveguides. *J. Sol-Gel Sci. Technol.* **2004**, *31*, 317–322. [[CrossRef](#)]
86. Sethi, S.; Bhattacharya, P.K. Characteristics and Device Applications of Erbium Doped III-V Semiconductors Grown by Molecular Beam Epitaxy. *J. Electron. Mater.* **1996**, *25*, 467–477. [[CrossRef](#)]
87. Pradhan, A.K.; Douglas, L.; Mustafa, H.; Mundle, R.; Hunter, D.; Bonner, C.E. Pulsed-laser deposited Er:ZnO films for 1.54 μm emission. *Appl. Phys. Lett.* **2007**, *90*, 072108. [[CrossRef](#)]
88. Popa, M.; Schmerber, G.; Toloman, D.; Gabor, M.S.; Mesaros, A.; Petrișor, T. Magnetic and Electrical Properties of Undoped and Holmium Doped ZnO Thin Films Grown by Sol-Gel Method. *Adv. Eng. Forum* **2013**, *8–9*, 301–308. [[CrossRef](#)]
89. Das, P.; Bathula, S.; Gollapudi, S. Evaluating the effect of grain size distribution on thermal conductivity of thermoelectric materials. *Nano Express* **2020**, *1*, 020036. [[CrossRef](#)]
90. Morais, E.A.; Scalvi, L.V.A.; Ribeiro, S.J.L.; Geraldo, V. Poole-Frenkel effect in Er doped SnO_2 thin films deposited by sol-gel-dip-coating. *Phys. Status Solidi A* **2005**, *202*, 301–308. [[CrossRef](#)]

91. Kityk, I.V.; Halyan, V.V.; Yukhymchuk, V.O.; Strelchuk, V.V.; Ivashchenko, I.A.; Zhydachevskyy, Y.; Suchocki, A.; Olekseyuk, I.D.; Kevshyn, A.H.; Piasecki, M. NIR and visible luminescence features of erbium doped Ga₂S₃–La₂S₃ glasses. *J. Non-Crystalline Solids* **2018**, *498*, 380–385. [[CrossRef](#)]
92. Yang, J.-H.; Gao, J.-F.; Yong, S.-L.; Ma, X.-L.; Liu, L.-J. Synthesis, characterization and optical studies on Sm²⁺-doped CdSe nanocrystals: A blueshift and fixed emission with high quantum yields. *Rare Met.* **2019**, *38*, 1097–1104. [[CrossRef](#)]
93. Han, J.; Wang, L.; Wong, S.S. Observation of Photoinduced Charge Transfer in Novel Luminescent CdSe Quantum Dot-CePO₄:Tb Metal Oxide Nanowire Composite Heterostructures. *J. Phys. Chem. C* **2014**, *118*, 5671–5682. [[CrossRef](#)]
94. Wang, M.; Zhang, Y.; Yao, Q.; Ng, M.; Lin, M.; Li, X.; Bhakoo, K.K.; Chang, A.Y.; Rosei, F.; Vetrone, F. Morphology Control of Lanthanide Doped NaGdF₄ Nanocrystals via One-Step Thermolysis. *Chem. Mater.* **2019**, *31*, 5160–5171. [[CrossRef](#)]

Disclaimer/Publisher’s Note: The statements, opinions and data contained in all publications are solely those of the individual author(s) and contributor(s) and not of MDPI and/or the editor(s). MDPI and/or the editor(s) disclaim responsibility for any injury to people or property resulting from any ideas, methods, instructions or products referred to in the content.